





**Electronic nematic order in the normal state of strontium ruthenate**Ryan S. Russell <sup>1</sup>, Hari P. Nair,<sup>2</sup> Kyle M. Shen,<sup>3,4</sup> Darrell G. Schlom <sup>2,4,5</sup> and John W. Harter <sup>1,\*</sup><sup>1</sup>*Materials Department, University of California, Santa Barbara, California 93106, USA*<sup>2</sup>*Department of Materials Science and Engineering, Cornell University, Ithaca, New York 14853, USA*<sup>3</sup>*Physics Department, Cornell University, Ithaca, New York 14853, USA*<sup>4</sup>*Kavli Institute at Cornell for Nanoscale Science, Ithaca, New York 14853, USA*<sup>5</sup>*Leibniz-Institut für Kristallzüchtung, 12489 Berlin, Germany* (Received 14 February 2023; revised 26 June 2023; accepted 24 July 2023; published 9 August 2023)

Despite significant achievements in characterizing the properties of  $\text{Sr}_2\text{RuO}_4$  over the last three decades, the precise nature of its electronic ground state is still unresolved. In this work, we provide a missing piece of the puzzle by uncovering evidence of electronic nematic order in the normal state of  $\text{Sr}_2\text{RuO}_4$ , revealed by ultrafast time-resolved optical dichroism measurements of uniaxially strained thin films. This nematic order, whose domains are aligned by the strain, spontaneously breaks the fourfold rotational symmetry of the crystal. The temperature dependence of the dichroism resembles an Ising-like order parameter, and optical pumping induces a coherent oscillation of its amplitude mode. The existence of electronic nematic order in the normal state of  $\text{Sr}_2\text{RuO}_4$  may have consequences for the form and mechanism of superconductivity in this material.

DOI: [10.1103/PhysRevB.108.L081105](https://doi.org/10.1103/PhysRevB.108.L081105)

**Introduction.** The study of  $\text{Sr}_2\text{RuO}_4$  entered a new era after the recent observation of a reduction in the Knight shift at the onset of superconductivity [1], which overturned the long-favored chiral  $p$ -wave triplet pairing scenario. Researchers are presently faced with an array of sometimes contradictory results, and it is clear that a fundamental piece of the  $\text{Sr}_2\text{RuO}_4$  puzzle is still missing [2]. It has long been believed that the normal state of  $\text{Sr}_2\text{RuO}_4$  is a conventional quasi-two-dimensional Fermi liquid with moderate correlations [2,3]. Evidence of any deviation from conventional Fermi liquid behavior would have significant consequences for theoretical proposals and the interpretation of experiments. In this work, we present such evidence. Motivated by recent transverse resistivity experiments [4], we use optical dichroism measurements of high-quality epitaxially strained thin films to uncover evidence of electronic nematic order in the normal state of  $\text{Sr}_2\text{RuO}_4$ .

Nematic order spontaneously breaks rotational symmetry while preserving translational symmetry. In a tetragonal crystal, nematicity results in a lowering of symmetry to an orthorhombic unit cell where the  $a$  and  $b$  directions become nonequivalent. The spontaneous nature of the symmetry breaking invariably leads to the formation of domains related by  $90^\circ$  rotations, whose average over long length scales retains the parent tetragonal symmetry. Thus, directly detecting nematic symmetry breaking with macroscopic probes generally requires stabilizing the formation of one type of domain, akin to structural detwinning. Uniaxial strain is an ideal external conjugate field by which one can achieve this effect. In the iron-based superconductors, for example, uniaxial strain has been used to study nematic order with optical, transport, and

photoemission experiments [5–9]. Here, we take advantage of uniaxial epitaxial strain to enable macroscopic transient optical reflectivity measurements of electronic nematic order in  $\text{Sr}_2\text{RuO}_4$ .

We study high-quality thin films of (001)-oriented  $\text{Sr}_2\text{RuO}_4$  grown by molecular beam epitaxy, as described in Ref. [10]. The films are 30 nm thick and coherently strained to (110)  $\text{NdGaO}_3$  single-crystal substrates [11], guaranteeing a clean, uniform strain field over the entire sample area. Transport measurements confirm the films are superconducting, with a critical temperature of  $T_c \approx 1.4$  K (see the Supplemental Material [12]).  $\text{NdGaO}_3$  induces a small uniaxial ( $B_{1g}$ ) strain of  $a/b - 1 \approx 0.3\%$  at low temperatures, where  $a$  and  $b$  are the in-plane lattice constants of the  $\text{Sr}_2\text{RuO}_4$  film. Specifically,  $a$  and  $b$  correspond to the  $[1\bar{1}0]$  and  $[001]$  spacings, respectively, of the (110)  $\text{NdGaO}_3$  substrate in the  $Pbnm$  setting [11] [Fig. 1(a)]. Strain has been used extensively in recent years to study the Lifshitz transition in  $\text{Sr}_2\text{RuO}_4$  and to enhance superconductivity [13–19]. We emphasize, however, that the magnitude of uniaxial strain that we employ is not sufficient to induce a Lifshitz transition (estimated in Ref. [19] to be  $\varepsilon_{xx} - \varepsilon_{yy} \approx 0.7\%$ ), and moreover, the epitaxial strain is biaxially compressive ( $-0.1\%$  in the  $a$  direction and  $-0.4\%$  in the  $b$  direction at low temperatures) relative to bulk  $\text{Sr}_2\text{RuO}_4$  [20,21], which is known to move the Fermi level away from the Van Hove singularity rather than towards it [14]. Thus, the effects that we measure are due to a relatively weak uniaxial perturbation of the electronic structure and are not expected to be driven by density of states enhancements or changes in band topology.

**Experimental results.** We first examine the static reflectivity anisotropy, defined as the ratio of reflectivity for light polarized along the  $a$  axis to that along the  $b$  axis. Figure 1(b) shows the measured anisotropy versus

\*Corresponding author: harter@ucsb.edu

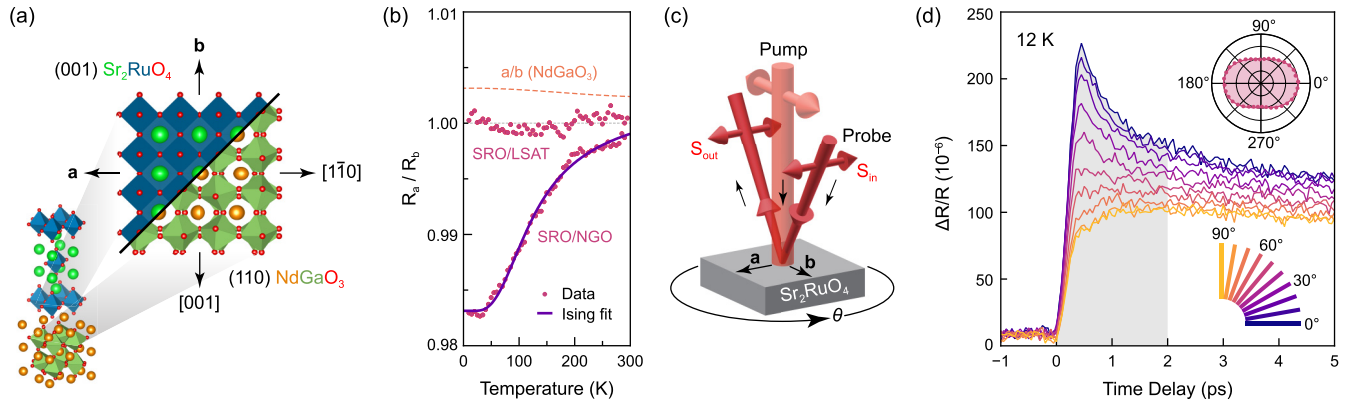


FIG. 1. Static and transient optical measurements. (a) Crystallographic directions in the film and substrate. For (001) Sr<sub>2</sub>RuO<sub>4</sub> on (110) NdGaO<sub>3</sub>, the  $a$  axis corresponds to  $[1\bar{1}0]$  NdGaO<sub>3</sub>, and the  $b$  axis corresponds to  $[001]$  NdGaO<sub>3</sub>. (b) Reflectivity anisotropy  $R_a/R_b$  versus temperature for films grown on NdGaO<sub>3</sub> (SRO/NGO) and LSAT (SRO/LSAT). A fit to an Ising model of nematic order is shown, as well as the lattice constant ratio  $a/b$  for films strained to NdGaO<sub>3</sub> (from Ref. [11]). (c) Illustration of the pump-probe experimental geometry. The pump and probe beams remain fixed in a cross-polarized configuration while the sample is rotated about its surface normal.  $\theta = 0^\circ$  when the probe is polarized along the  $a$  axis (as shown) and  $\theta = 90^\circ$  when polarized along the  $b$  axis. (d) Raw transient reflectivity curves for several values of  $\theta$  at 12 K. A clear anisotropy is observed in the picosecond-scale transient response. The inset shows a polar plot of  $\Delta R/R$  integrated from 0 to 2 ps (gray shaded region).

temperature using a probe wavelength of 800 nm, where a striking dichroism is apparent. We find a decrease in reflectivity along the (long)  $a$  axis relative to the (short)  $b$  axis, which becomes more pronounced at lower temperatures. At the lowest temperatures, the maximum reflectivity anisotropy is 1.7%, more than 5 times larger than the uniaxial strain imposed by the substrate (0.3%). Similar behavior has been observed in detwinned FeSe, where the reflectivity anisotropy was taken as a proxy for the nematic order parameter [9]. To eliminate the possibility that the dichroism is merely due to structural orthorhombicity, we include in Fig. 1 the temperature-dependent lattice constant ratio  $a/b$  for films strained to NdGaO<sub>3</sub>. If the anisotropy is due to simple  $a \neq b$  structural effects, we would expect a linear proportionality with the substrate orthorhombicity (see the Supplemental Material [12]). Instead, we observe the dichroism grow by an order of magnitude upon cooling, while the substrate orthorhombicity increases by only 30%. As a control, we also measure the reflectivity of Sr<sub>2</sub>RuO<sub>4</sub> grown on (001) (LaAlO<sub>3</sub>)<sub>0.29</sub>(SrTa<sub>1/2</sub>Al<sub>1/2</sub>O<sub>3</sub>)<sub>0.71</sub> (LSAT), which is tetragonal and induces no uniaxial strain ( $a = b$ ) [22]. In this case, we detect no appreciable dichroism. Our static optical anisotropy measurements suggest that the electronic structure of Sr<sub>2</sub>RuO<sub>4</sub> possesses either spontaneous nematic order (scenario I) or a large nematic susceptibility (scenario II). In scenario I, an electronic instability results in the formation of microscopic nematic domains, with one orientation favored by the uniaxial strain over the other. This imbalance induces a net macroscopic anisotropy in the optical response. In scenario II, the weak uniaxial strain drives a strong electronic nematic response via a large nematic susceptibility. Without the strain, however, the electronic structure would retain tetragonal symmetry at all temperatures. Both scenarios are consistent with an absence of dichroism in films grown on LSAT.

Now that signatures of electronic nematic order in the optical dichroism have been established, we next turn to

measuring the ultrafast response of the order. As we will show, this reveals much larger signatures of nematicity than the static reflectivity and enables the extraction of dynamical information. We use a standard pump-probe transient reflectivity technique to measure changes in the dichroism induced by an ultrafast ( $\sim 50$  fs) pump pulse with a wavelength of 760 nm and fluence  $\sim 25 \mu\text{J}/\text{cm}^2$ . To eliminate any possible anisotropy due to the polarization of the pump, we keep the pump and probe pulses fixed in a cross-polarized configuration and rotate the sample about its surface normal [Fig. 1(c)]. Like the static reflectivity, we uncover a pronounced anisotropy of the transient response. Figure 1(d) shows raw transients of the relative change in reflectivity  $\Delta R/R$  versus pump-probe time delay at 12 K for several angles between the  $a$  axis ( $0^\circ$ ) and the  $b$  axis ( $90^\circ$ ). A clear breaking of tetragonal symmetry is apparent: For optical polarization parallel to the  $a$  axis, we observe a sharp peak in  $\Delta R/R$  that decays over an  $\sim 1$  ps timescale, whereas for polarization parallel to the  $b$  axis, we observe only a flat step. This nematic ( $C_4 \rightarrow C_2$ ) symmetry breaking can be seen more clearly in a polar plot of the area under the curve [inset in Fig. 1(d)]. While the static reflectivity shows a modest 1.7% anisotropy, the transient reflectivity anisotropy exceeds 100%. Ultrafast optical anisotropies of this magnitude are routinely observed in the nematic phase of iron-based superconductors [23–27]. Sr<sub>2</sub>RuO<sub>4</sub> is a multiband system with strong hybridization between the three Ru  $t_{2g}$  orbitals and six O  $p_{x,y}$  orbitals, and photon absorption at our pump energy (1.6 eV) results from a mixture of intraband and interband electronic transitions [28]. Strongest absorption is expected between occupied  $d_{xz,yz}$  states (forming the  $\alpha$  and  $\beta$  bands) and unoccupied  $d_{x^2-y^2}$  states. These directly photoexcited “hot” electrons will subsequently thermalize with the  $d_{xy}$  electrons forming the  $\gamma$  band, which contains the electronic states with the most relevance to nematic order (see the microscopic model discussed below). Our experiments are carried out in the low excitation density limit, and the conventional expectation

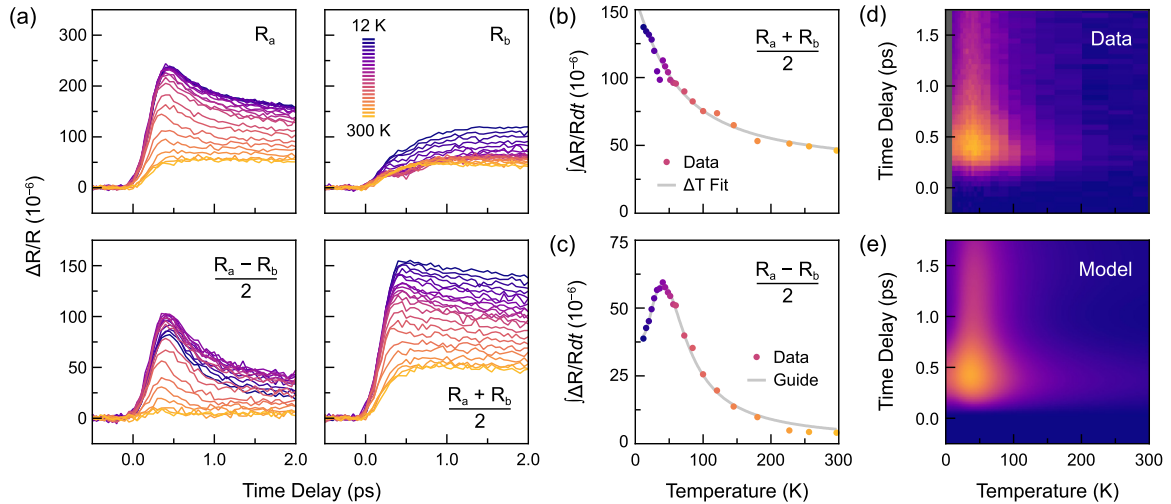


FIG. 2. Temperature dependence of transient reflectivity. (a)  $\Delta R/R$  for selected temperatures between 12 and 300 K for polarization along the  $a$  axis (top left) and  $b$  axis (top right), their difference (bottom left), and their sum (bottom right). (b) Temperature dependence of the average value of  $\Delta(R_a + R_b)/2R$  between 1.5 and 2 ps, representing the isotropic component of the transient response. The response monotonically decreases with increasing temperature. The gray line is a fit to the sample temperature change. (c) Temperature dependence of the average value of  $\Delta(R_a - R_b)/2R$  between 0 and 2 ps, representing the nematic component of the transient response. An unusual nonmonotonic behavior is observed. (d) Two-dimensional joint time delay and temperature dependence of  $\Delta(R_a - R_b)/2R$ . (e) Corresponding depiction generated by fitting to the Ising nematic model.

that electron-phonon thermalization is slower than electron-electron thermalization does not necessarily hold [29]. More specifically, hot phonons may be generated through rapid thermalization with the hot electrons, followed by a slower thermalization with the rest of the system, as has been observed in time-resolved studies of the cuprates [30]. As we discuss in more detail below, we see evidence of this slower electron-electron thermalization in the thermal response of the nematic degrees of freedom.

Figure 2(a) shows transient reflectivity measurements at several temperatures between 12 and 300 K for polarization along the  $a$  axis ( $R_a$ ) and  $b$  axis ( $R_b$ ). To isolate temperature-dependent changes in the anisotropy from other effects, we also show the difference  $(R_a - R_b)$  and sum  $(R_a + R_b)$ . We see that the sharp peak in  $\Delta R/R$  is entirely due to the nematicity of the material, while the flat step after time zero represents the isotropic component of the optical response. Moreover, while the isotropic response monotonically decreases with increasing temperature [Fig. 2(b)], we uncover an unusual nonmonotonic temperature dependence of the nematic component of the response [Fig. 2(c)]. The isotropic transient response is likely caused by an increase in temperature  $\Delta T$  after absorption of the pump. Assuming each pump pulse deposits a fixed energy  $\Delta E$  into the electronic subsystem (heat capacity  $C = \gamma T$ ), it follows that  $\Delta T_{\max}(T) = \sqrt{T^2 + (2\Delta E/\gamma)} - T$ . Using the value of  $\gamma$  from Ref. [31] and  $\Delta E$  calculated from our fluence, we find  $(2\Delta E/\gamma) \approx (80 \text{ K})^2$  (see the Supplemental Material [12]). A function of the form  $g(T) = \alpha + \beta \Delta T_{\max}(T)$  fits the isotropic component extremely well [gray line in Fig. 2(b)]. We use this fact to scale the data at each temperature to match  $g(T)$  and correct for laser fluctuations during the experiment, where, for example, the two data points near  $\sim 35$  K are otherwise

anomalously low. This normalization procedure is used for the remainder of our analysis.

*Ising nematic model of data.* Saturation at low temperatures is evident in the static dichroism [Fig. 1(b)], resembling an Ising-like order parameter. To quantitatively analyze the data, we therefore develop a heuristic mean-field Ising model of the nematic order, which can describe both scenarios discussed above. Within the model, we define an order parameter  $\phi$  that takes a value of  $+1$  or  $-1$ , corresponding to a nematic director oriented along the  $a$  or  $b$  axis, respectively. The Hamiltonian is

$$\mathcal{H} = -\frac{1}{2} \sum_{i,j} U(\mathbf{r}_i - \mathbf{r}_j) \phi_i \phi_j - F \sum_i \phi_i,$$

where  $i$  and  $j$  label unit cells,  $U(\mathbf{r})$  is the interaction energy (related to the stiffness of the nematic order), and  $F$  is the uniaxial strain field, which favors  $+1$  domains over  $-1$  domains. Within mean-field theory, the average order parameter  $\langle \phi \rangle$  satisfies the self-consistency equation

$$\langle \phi \rangle = \tanh \left( \frac{U \langle \phi \rangle + F}{k_B T} \right),$$

where  $U = \sum_i U(\mathbf{r}_i)/2 = k_B T_c$  defines the critical temperature of the nematic phase transition. We assume the measured optical anisotropy is proportional to the order parameter ( $R_a/R_b - 1 \propto \langle \phi \rangle$ ) and fit the data to this functional form. The least-squares fit, included in Fig. 1(b), yields the parameters  $U = 53 \pm 8$  K and  $F = 53 \pm 7$  K. Excellent agreement with the data is achieved despite the relative simplicity of our model. Taking it at face value, the model predicts a critical temperature of  $T_c \approx 50$  K, where global nematic order spontaneously condenses following scenario I. In reality, this

transition is spread over a wide temperature range due to the large magnitude of the symmetry-breaking uniaxial strain field. Scenario II, where nematic order does not occur without strain, would require  $U \leq 0$ , which is not consistent with our data. Based on the success of this simple Ising nematic model, we will continue to use it to quantitatively analyze the data.

Figure 1(b) shows that the onset of nematic order reduces the optical reflectivity along the  $a$  axis. After the pump pulse, this reflectivity increases. It follows that the effect of the pump is to suppress the nematic order, likely through a transient increase in temperature. To model this, we assume the dichroism is proportional to the nematic order parameter  $\phi$ . The measured change in dichroism is therefore proportional to the change in  $\phi$ :

$$\Delta(R_a - R_b)/R \propto (1 + \delta)\phi(T + \Delta T) - \phi(T),$$

where  $\phi(T)$  is the equilibrium value of the order parameter at the measurement temperature  $T$ ,  $\Delta T$  is the increase in electronic temperature after absorption of the pump energy, and  $\delta < 0$  represents a nonthermal suppression of the order parameter amplitude by the pump pulse. The previously developed Ising model provides an expression for  $\phi(T)$ . The temperature increase  $\Delta T$  is not necessarily instantaneous. Instead, we allow the temperature of the electrons to rise to some time-dependent fraction  $0 \leq f(t) \leq 1$  of  $\Delta T_{\max}$  [ $\Delta T(t) = f(t)\Delta T_{\max}$ ]. With this model, we fit the transient optical data at all time delays and all temperatures simultaneously. The fit includes three global parameters ( $U$ ,  $F$ , and a fixed scaling factor) and two time-dependent parameters [ $\delta(t)$  and  $f(t)$ ]. The results of the fit, shown in Fig. 3(a), are excellent ( $R^2 = 0.994$ ).

A number of salient points are uncovered by the fit: (1) The nonmonotonic temperature dependence of the dichroism [Fig. 2(c)] is a result of the flattening of the nematic order parameter at low temperatures ( $d\phi/dT \rightarrow 0$  as  $T \rightarrow 0$ ), which reduces the effect of pump heating. At the lowest temperatures, the pump-induced change in temperature  $\Delta T$  does not induce a large change in the order parameter  $\Delta\phi$ , so the measured  $\Delta(R_a - R_b)/R$  correspondingly drops. (2) Uncertainties in the fit parameters  $U$  and  $F$  are correlated, which is a result of their coupled influence on  $\phi(T)$ . The  $F$ -test-derived confidence regions displayed in Fig. 3(c), however, show that  $U > 0$  with high confidence. Crucially, if the uniaxial strain were to be removed ( $F \rightarrow 0$ ), spontaneous nematic order would still occur within the model at  $T_c = U$ . Within the applicability of the model, this implies that the nematic order we observe is spontaneous (scenario I). We note that a more realistic model, such as one that includes a temperature-dependent proportionality constant or a nonlinear dependence on the conjugate strain field, may alter this interpretation. (3) While we extract a value for  $F$  similar to that of the static measurement (46 versus 53 K), the value of  $U$  is smaller (23 versus 53 K). We conjecture that repeatedly exciting the sample with high-fluence optical pulses does not allow it to completely return to equilibrium, causing a net suppression of the order parameter. This subsequently renormalizes the average interaction energy  $U$ . (4) Figure 3(c) shows that the nematic electron temperature rises to  $\sim 50\%$  of the maximum calculated increase  $\Delta T_{\max}$  within  $\sim 0.6$  ps. This is consistent with a scenario in which the pump energy is first absorbed

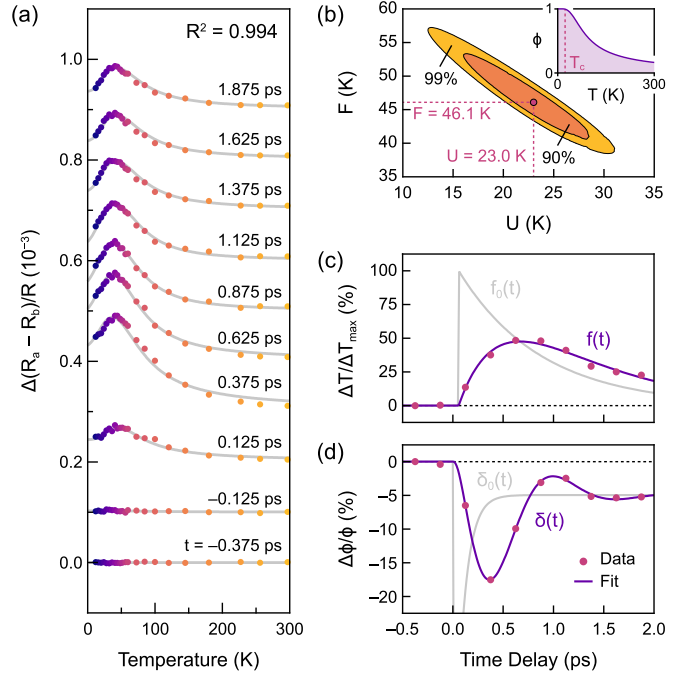


FIG. 3. Ising model fit of optical anisotropy. (a)  $\Delta(R_a - R_b)/R$  versus temperature for selected time delays after the pump pulse. Curves are offset by  $10^{-4}$ . Gray lines show the global fit to the Ising nematic model, as described in the text. (b) Confidence regions for the Ising parameters  $U$  and  $F$  computed through an  $F$ -test.  $U > 0$  with greater than 99% confidence, implying the existence of spontaneous nematic order. The inset shows the order parameter  $\phi(T)$  together with the critical temperature  $T_c$  for spontaneous nematic order when  $F = 0$ . (c) Electronic temperature increase versus time delay as a fraction of the calculated maximum increase. Also shown is a fit to the solution of the heat equation  $df/dt = k(f_0 - f)$  (purple curve) with the background electronic temperature  $f_0$  (gray curve). (d) Relative suppression of the nematic order versus time delay, showing a coherent oscillation of the order parameter amplitude. Also shown is a fit to a damped harmonic oscillator (purple curve) with a pump-induced displacement of the equilibrium amplitude (gray curve).

by background “hot” electrons during the pulse ( $\sim 50$  fs) and then transferred at a slower timescale to the nematic degrees of freedom via thermal equilibration mediated by electron-electron interactions. To make this picture more quantitative, we fit  $f(t)$  to the heat equation  $df/dt = k(f_0 - f)$  (see the Supplemental Material [12]), where  $f_0(t) = e^{-t/\tau}$  represents the temperature of the hot electron (and potentially hot phonon [30]) background, with timescale  $\tau$  for equilibration with the rest of the system. We find excellent agreement with the data for  $\tau = 0.82$  ps and  $k^{-1} = 0.47$  ps. The latter parameter represents a relatively slow thermalization between the hot particles and the nematic order. This slow thermalization is expected in the low excitation density limit due to a reduced phase space for electron-electron scattering by Pauli blocking [29]. (5) The nonthermal suppression of the order parameter after the pump pulse [Fig. 3(d)] reveals a coherent oscillation, which can be understood with a damped harmonic oscillator model:  $d^2\delta/dt^2 + 2\gamma d\delta/dt + \omega_0^2(\delta - \delta_0) = 0$ , where  $\gamma$  is the damping rate,  $\omega_0$  is the natural frequency,



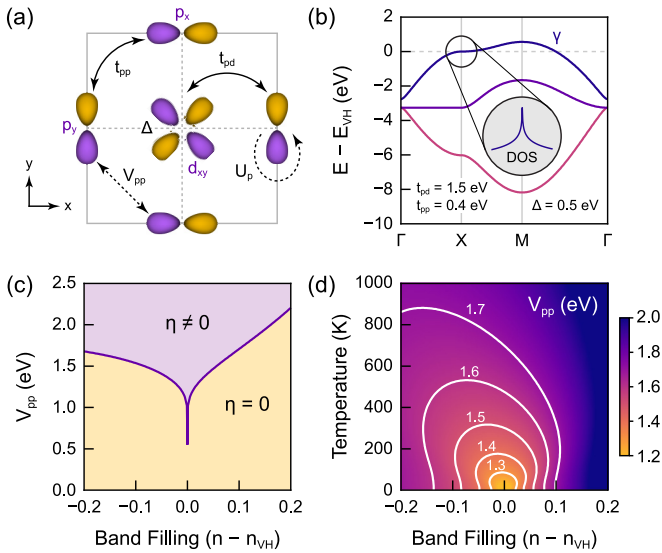


FIG. 4. Microscopic model of nematic order in  $\text{Sr}_2\text{RuO}_4$ . (a) Unit cell of the  $\text{RuO}_2$  plane showing the three-orbital basis (Ru  $d_{xy}$  and O  $p_x$  and  $p_y$ ) of the Emery model. Hopping integrals (solid lines) and interaction parameters (dashed lines) are defined following Ref. [34]. (b) Resulting tight-binding band structure, with parameters taken from Ref. [35]. (c) Interaction-filling phase diagram showing the critical value of  $V_{pp}$  necessary to produce a nematic ground state ( $\eta \neq 0$ ). (d) Temperature-filling phase diagram for different values of  $V_{pp}$ . (c) and (d) were calculated for  $U_p = 4.4$  eV [35].

and  $\delta_0$  is the pump-induced displacement of the order parameter amplitude. A solution to this equation fits the data well if  $\delta_0(t) = \alpha e^{-t/\tau} + \beta$ , representing a sharp impulsive suppression at  $t = 0$  followed by a rapid recovery ( $\tau = 0.09$  ps) to a displaced equilibrium amplitude  $\beta = -5.0\%$  relative to the initial value [gray curve in Fig. 3(d)]. We extract a frequency  $\omega_0/2\pi = 0.89$  THz for the nematic amplitude mode.

**Microscopic model.** The foregoing optical experiments suggest that  $\text{Sr}_2\text{RuO}_4$  supports a high-temperature Ising-like nematic order parameter with an order-disorder phase transition below  $\sim 50$  K. To put forth a possible microscopic origin for this order, we turn to the Emery model, first used to describe hole doping of  $\text{CuO}_2$  planes in cuprate superconductors away from half filling [32]. Here, we use the model to study intra-unit-cell nematic order in  $\text{RuO}_2$  planes with fillings adjacent to the Van Hove singularity of the  $\gamma$  band [33]. Our mean-field analysis closely follows Ref. [34] (see the Supplemental Material [12]). Figure 4(a) shows the hopping and interaction parameters defined within the model, and Fig. 4(b) shows the resulting band structure. Of central importance are the Coulomb repulsion between neighboring oxygen  $p$  orbitals  $V_{pp}$ , which favors a nematic charge order  $\eta = n_x^p - n_y^p$  with different electron densities on the  $p_x$  and  $p_y$  orbitals, and the Van Hove singularity of the  $\gamma$  band at the  $X$  point, which leads to a diverging density of states that supports electronic instabilities by reducing the energy cost to redistribute orbital density. Figure 4(c) shows the mean-field ground state phase diagram as a function of  $V_{pp}$  and filling. A nematic phase is stabilized for sufficiently large values of  $V_{pp}$  that depend on the proximity to the Van Hove filling.

Bulk  $\text{Sr}_2\text{RuO}_4$  has  $n - n_{\text{VH}} \approx -0.2$  [33], which requires an interaction strength  $V_{pp} > 1.7$  eV to stabilize nematic order. The full temperature-filling phase diagram is displayed in Fig. 4(d), where it is seen that such order, if it exists, condenses well above room temperature. The model shows that  $\text{Sr}_2\text{RuO}_4$  is exceptionally close to a nematic instability and offers a plausible microscopic picture of an Ising-like ( $\eta = \pm\eta_0$ ) nematic charge order. We conjecture that at high temperatures this nematicity is spatially disordered at the nanoscale but shows an order-disorder phase transition to a globally nematic state at lower temperatures.

**Conclusion.** In conclusion, optical dichroism measurements of epitaxially strained thin films strongly support the existence of electronic nematic order in  $\text{Sr}_2\text{RuO}_4$ . By fitting our data to a simple Ising model, we conjecture that this order emerges spontaneously at low temperatures through an order-disorder transition, rather than through a large nematic susceptibility. Outside the framework of this model, however, the possibility remains that the nematic order we observe originates through a large, but finite, nematic susceptibility. Our results corroborate the angle-resolved transverse resistivity measurements that first uncovered electronic nematicity in  $\text{Sr}_2\text{RuO}_4$  [4]. While electrical transport and optical reflectivity are disparate probes operating at different energy scales, they both show clear signatures of twofold electronic anisotropy. Furthermore, although transport can be sensitive to nonlocal effects such as defect scattering, especially in a material with ostensible microscopic nematic domains, optical reflectivity is a local, bulk-sensitive probe. Our findings also offer a different perspective on the Fermi liquid crossover at  $T_{\text{FL}} \sim 40$  K observed by Hall transport [36–38], optical spectroscopy [28], and nuclear magnetic resonance [39,40]. We speculate that the crossover is directly related to nematicity, which appears to develop at the same temperature. Indeed, such a Fermi liquid crossover has been theoretically shown to emerge in the vicinity of an Ising nematic quantum critical point [41–43]. Nematic order also offers a natural explanation for the checkerboard charge order observed at the surface of  $\text{Sr}_2\text{RuO}_4$  by scanning tunneling microscopy [44]. Rather than surface nematic order emerging as a secondary effect, we find it likely that the checkerboard charge order is the secondary response, emerging from a combination of bulk nematicity and surface octahedral rotations. An important open question is to what extent electronic nematic order in the normal state of  $\text{Sr}_2\text{RuO}_4$  influences the likelihood of different forms of superconductivity at lower temperatures. Future experimental and theoretical work is necessary to address this principal question.

**Acknowledgments.** We thank Dr. L. Miao for performing electrical resistivity measurements. This work was primarily supported by the U.S. Department of Energy, Office of Basic Energy Sciences under Award No. DE-SC0019414. Thin-film synthesis was funded in part by the Gordon and Betty Moore Foundation's EPiQS Initiative through Grants No. GBMF3850 and No. GBMF9073 to Cornell University. Substrate preparation was, in part, facilitated by the Cornell NanoScale Facility, a member of the National Nanotechnology Coordinated Infrastructure (NNCI), which is supported by the National Science Foundation (Grant No. NNCI-2025233). Additional support was provided by AFOSR Grant No. FA9550-21-1-0168.

- [1] A. Pustogow, Y. Luo, A. Chronister, Y.-S. Su, D. A. Sokolov, F. Jerzembeck, A. P. Mackenzie, C. W. Hicks, N. Kikugawa, S. Raghu, E. D. Bauer, and S. E. Brown, Constraints on the superconducting order parameter in  $\text{Sr}_2\text{RuO}_4$  from oxygen-17 nuclear magnetic resonance, *Nature (London)* **574**, 72 (2019).
- [2] A. P. Mackenzie, T. Scaffidi, C. W. Hicks, and Y. Maeno, Even odder after twenty-three years: The superconducting order parameter puzzle of  $\text{Sr}_2\text{RuO}_4$ , *npj Quantum Mater.* **2**, 40 (2017).
- [3] A. P. Mackenzie and Y. Maeno, The superconductivity of  $\text{Sr}_2\text{RuO}_4$  and the physics of spin-triplet pairing, *Rev. Mod. Phys.* **75**, 657 (2003).
- [4] J. Wu, H. P. Nair, A. T. Bollinger, X. He, I. Robinson, N. J. Schreiber, K. M. Shen, D. G. Schlom, and I. Božović, Electronic nematicity in  $\text{Sr}_2\text{RuO}_4$ , *Proc. Natl. Acad. Sci. USA* **117**, 10654 (2020).
- [5] A. Dusza, A. Lucarelli, F. Pfuner, J.-H. Chu, I. R. Fisher, and L. Degiorgi, Anisotropic charge dynamics in detwinned  $\text{Ba}(\text{Fe}_{1-x}\text{Co}_x)_2\text{As}_{1-x}$ , *Europhys. Lett.* **93**, 37002 (2011).
- [6] M. A. Tanatar, E. C. Blomberg, A. Kreyssig, M. G. Kim, N. Ni, A. Thaler, S. L. Bud'ko, P. C. Canfield, A. I. Goldman, I. I. Mazin, and R. Prozorov, Uniaxial-strain mechanical detwinning of  $\text{CaFe}_2\text{As}_2$  and  $\text{BaFe}_2\text{As}_2$  crystals: Optical and transport study, *Phys. Rev. B* **81**, 184508 (2010).
- [7] J.-H. Chu, J. G. Analytis, K. De Greve, P. L. McMahon, Z. Islam, Y. Yamamoto, and I. R. Fisher, In-plane resistivity anisotropy in an underdoped iron arsenide superconductor, *Science* **329**, 824 (2010).
- [8] M. Yi, D. Lu, J.-H. Chu, J. G. Analytis, A. P. Sorini, A. F. Kemper, B. Moritz, S.-K. Mo, R. G. Moore, M. Hashimoto, W.-S. Lee, Z. Hussain, T. D. Devereaux, I. R. Fisher, and Z.-X. Shen, Symmetry-breaking orbital anisotropy observed for detwinned  $\text{Ba}(\text{Fe}_{1-x}\text{Co}_x)_2\text{As}_2$  above the spin density wave transition, *Proc. Natl. Acad. Sci. USA* **108**, 6878 (2011).
- [9] M. Chinotti, A. Pal, L. Degiorgi, A. E. Böhmer, and P. C. Canfield, Optical anisotropy in the electronic nematic phase of FeSe, *Phys. Rev. B* **96**, 121112(R) (2017).
- [10] H. P. Nair, J. P. Ruf, N. J. Schreiber, L. Miao, M. L. Grandon, D. J. Baek, B. H. Goodge, J. P. C. Ruff, L. F. Kourkoutis, K. M. Shen, and D. G. Schlom, Demystifying the growth of superconducting  $\text{Sr}_2\text{RuO}_4$  thin films, *APL Mater.* **6**, 101108 (2018).
- [11] D. Savytskii, L. Vasylechko, A. Senyshyn, A. Matkovskii, C. Bähz, M. L. Sanjuán, U. Bismayer, and M. Berkowski, Low-temperature structural and Raman studies on rare-earth gallates, *Phys. Rev. B* **68**, 024101 (2003).
- [12] See Supplemental Material at <http://link.aps.org/supplemental/10.1103/PhysRevB.108.L081105> for experimental methods, nematicity across several relaxation timescales, measurements of film on an LSAT substrate, calculation of pump-induced temperature change, derivation of the heat equation, and a microscopic model of nematic charge order.
- [13] C. W. Hicks, D. O. Brodsky, E. A. Yelland, A. S. Gibbs, J. A. N. Bruin, M. E. Barber, S. D. Edkins, K. Nishimura, S. Yonezawa, Y. Maeno, and A. P. Mackenzie, Strong increase of  $T_c$  of  $\text{Sr}_2\text{RuO}_4$  under both tensile and compressive strain, *Science* **344**, 283 (2014).
- [14] B. Burganov, C. Adamo, A. Mulder, M. Uchida, P. D. C. King, J. W. Harter, D. E. Shai, A. S. Gibbs, A. P. Mackenzie, R. Uecker, M. Bruetzsch, M. R. Beasley, C. J. Fennie, D. G. Schlom, and K. M. Shen, Strain Control of Fermiology and Many-Body Interactions in Two-Dimensional Ruthenates, *Phys. Rev. Lett.* **116**, 197003 (2016).
- [15] A. Steppke, L. Zhao, M. E. Barber, T. Scaffidi, F. Jerzembeck, H. Rosner, A. S. Gibbs, Y. Maeno, S. H. Simon, A. P. Mackenzie, and C. W. Hicks, Strong peak in  $T_c$  of  $\text{Sr}_2\text{RuO}_4$  under uniaxial pressure, *Science* **355**, eaaf9398 (2017).
- [16] V. Sunko, E. A. Morales, I. Marković, M. E. Barber, D. Milosavljević, F. Mazzola, D. A. Sokolov, N. Kikugawa, C. Cacho, P. Dudin, H. Rosner, C. W. Hicks, P. D. C. King, and A. P. Mackenzie, Direct observation of a uniaxial stress-driven Lifshitz transition in  $\text{Sr}_2\text{RuO}_4$ , *npj Quantum Mater.* **4**, 46 (2019).
- [17] V. Grinenko, S. Ghosh, R. Sarkar, J.-C. Orain, A. Nikitin, M. Elender, D. Das, Z. Guguchia, F. Brückner, M. E. Barber, J. Park, N. Kikugawa, D. A. Sokolov, J. S. Bobowski, T. Miyosho, Y. Maeno, A. P. Mackenzie, H. Luetkens, C. W. Hicks, and H.-H. Klauss, Split superconducting and time-reversal symmetry-breaking transitions in  $\text{Sr}_2\text{RuO}_4$  under stress, *Nat. Phys.* **17**, 748 (2021).
- [18] Y.-S. Li, N. Kikugawa, D. A. Sokolov, F. Jerzembeck, A. S. Gibbs, Y. Maeno, C. W. Hicks, J. Schmalian, M. Nicklas, and A. P. Mackenzie, High-sensitivity heat-capacity measurements on  $\text{Sr}_2\text{RuO}_4$  under uniaxial pressure, *Proc. Natl. Acad. Sci. USA* **118**, e2020492118 (2021).
- [19] M. E. Barber, F. Lechermann, S. V. Streltsov, S. L. Skornyakov, S. Ghosh, B. J. Ramshaw, N. Kikugawa, D. A. Sokolov, A. P. Mackenzie, C. W. Hicks, and I. I. Mazin, Role of correlations in determining the Van Hove strain in  $\text{Sr}_2\text{RuO}_4$ , *Phys. Rev. B* **100**, 245139 (2019).
- [20] T. Vogt and D. J. Buttrey, Low-temperature structural behavior of  $\text{Sr}_2\text{RuO}_4$ , *Phys. Rev. B* **52**, R9843 (1995).
- [21] O. Chmaissem, J. D. Jorgensen, H. Shaked, S. Ikeda, and Y. Maeno, Thermal expansion and compressibility of  $\text{Sr}_2\text{RuO}_4$ , *Phys. Rev. B* **57**, 5067 (1998).
- [22] M. Steins, J. Doerschel, and P. Reiche, Crystal structure of aluminium lanthanum strontium tantalum oxide,  $(\text{La}_{0.272}\text{Sr}_{0.728})(\text{Al}_{0.648}\text{Ta}_{0.352})\text{O}_3$ , *Z. Kristallogr. - New Cryst. Struct.* **212**, 77 (1997).
- [23] L. Stojchevska, T. Mertelj, J.-H. Chu, I. R. Fisher, and D. Mihailovic, Doping dependence of femtosecond quasiparticle relaxation dynamics in  $\text{Ba}(\text{Fe}, \text{Co})_2\text{As}_2$  single crystals: Evidence for normal-state nematic fluctuations, *Phys. Rev. B* **86**, 024519 (2012).
- [24] C.-W. Luo, P. C. Cheng, S.-H. Wang, J.-C. Chiang, J.-Y. Lin, K.-H. Wu, J.-Y. Juang, D. A. Chareev, O. S. Volkova, and A. N. Vasiliev, Unveiling the hidden nematicity and spin subsystem in FeSe, *npj Quantum Mater.* **2**, 32 (2017).
- [25] S. Liu, C. Zhang, Q. Deng, H. Wen, J. Li, E. E. M. Chia, X. Wang, and M. Xiao, Transient electronic anisotropy in overdoped  $\text{NaFe}_{1-x}\text{Co}_x\text{As}$  superconductors, *Phys. Rev. B* **97**, 020505(R) (2018).
- [26] E. Thewalt, I. M. Hayes, J. P. Hinton, A. Little, S. Patankar, L. Wu, T. Helm, C. V. Stan, B. Tamura, J. G. Analytis, and J. Orenstein, Imaging Anomalous Nematic Order and Strain in Optimally Doped  $\text{BaFe}_2(\text{As}, \text{P})_2$ , *Phys. Rev. Lett.* **121**, 027001 (2018).
- [27] M.-C. Lee, I. Kwak, Y. Lee, B. Lee, B. C. Park, T. Wolf, T. W. Noh, and K. Kim, Nematic response revealed by coherent phonon oscillations in  $\text{BaFe}_2\text{As}_2$ , *Phys. Rev. B* **105**, 024501 (2022).

- [28] D. Stricker, J. Mravlje, C. Berthod, R. Fittipaldi, A. Vecchione, A. Georges, and D. van der Marel, Optical Response of  $\text{Sr}_2\text{RuO}_4$  Reveals Universal Fermi-Liquid Scaling and Quasiparticles Beyond Landau Theory, *Phys. Rev. Lett.* **113**, 087404 (2014).
- [29] M. Obergfell and J. Demsar, Tracking the Time Evolution of the Electron Distribution Function in Copper by Femtosecond Broadband Optical Spectroscopy, *Phys. Rev. Lett.* **124**, 037401 (2020).
- [30] L. Perfetti, P. A. Loukakos, M. Lisowski, U. Bovensiepen, H. Eisaki, and M. Wolf, Ultrafast Electron Relaxation in Superconducting  $\text{Bi}_2\text{Sr}_2\text{CaCu}_2\text{O}_{8+\delta}$  by Time-Resolved Photoelectron Spectroscopy, *Phys. Rev. Lett.* **99**, 197001 (2007).
- [31] A. P. Mackenzie, S.-I. Ikeda, Y. Maeno, T. Fujita, S. R. Julian, and G. G. Lonzarich, The Fermi surface topography of  $\text{Sr}_2\text{RuO}_4$ , *J. Phys. Soc. Jpn.* **67**, 385 (1998).
- [32] V. J. Emery, Theory of High- $T_c$  Superconductivity in Oxides, *Phys. Rev. Lett.* **58**, 2794 (1987).
- [33] K. M. Shen, N. Kikugawa, C. Bergemann, L. Balicas, F. Baumberger, W. Meevasana, N. J. C. Ingle, Y. Maeno, Z.-X. Shen, and A. P. Mackenzie, Evolution of the Fermi Surface and Quasiparticle Renormalization through a Van Hove Singularity in  $\text{Sr}_{2-y}\text{La}_y\text{RuO}_4$ , *Phys. Rev. Lett.* **99**, 187001 (2007).
- [34] M. H. Fischer and E.-A. Kim, Mean-field analysis of intra-unit-cell order in the Emery model of the  $\text{CuO}_2$  plane, *Phys. Rev. B* **84**, 144502 (2011).
- [35] K. Rościszewski and A. M. Oleś, Charge-transfer model for the electronic structure of layered ruthenates, *Phys. Rev. B* **91**, 155137 (2015).
- [36] N. Shirakawa, K. Murata, Y. Nishihara, S. Nishizaki, Y. Maeno, T. Fujita, J. G. Bednorz, F. Lichtenberg, and N. Hamada, Novel Hall-coefficient behavior in superconducting  $\text{Sr}_2\text{RuO}_4$ , *J. Phys. Soc. Jpn.* **64**, 1072 (1995).
- [37] A. P. Mackenzie, N. E. Hussey, A. J. Diver, S. R. Julian, Y. Maeno, S. Nishizaki, and T. Fujita, Hall effect in the two-dimensional metal  $\text{Sr}_2\text{RuO}_4$ , *Phys. Rev. B* **54**, 7425 (1996).
- [38] M. Zingl, J. Mravlje, M. Aichhorn, O. Parcollet, and A. Georges, Hall coefficient signals orbital differentiation in the Hund's metal  $\text{Sr}_2\text{RuO}_4$ , *npj Quantum Mater.* **4**, 35 (2019).
- [39] T. Imai, A. W. Hunt, K. R. Thurber, and F. C. Chou,  $^{17}\text{O}$  NMR Evidence for Orbital Dependent Ferromagnetic Correlations in  $\text{Sr}_2\text{RuO}_4$ , *Phys. Rev. Lett.* **81**, 3006 (1998).
- [40] A. Chronister, M. Zingl, A. Pustogow, Y. Luo, D. A. Sokolov, F. Jerzembeck, N. Kikugawa, C. W. Hicks, J. Mravlje, E. D. Bauer, J. D. Thompson, A. P. Mackenzie, A. Georges, and S. E. Brown, Tuning the Fermi liquid crossover in  $\text{Sr}_2\text{RuO}_4$  with uniaxial stress, *npj Quantum Mater.* **7**, 113 (2022).
- [41] X. Wang and E. Berg, Scattering mechanisms and electrical transport near an Ising nematic quantum critical point, *Phys. Rev. B* **99**, 235136 (2019).
- [42] V. S. de Carvalho and R. M. Fernandes, Resistivity near a nematic quantum critical point: Impact of acoustic phonons, *Phys. Rev. B* **100**, 115103 (2019).
- [43] L. E. Vieira, V. S. de Carvalho, and H. Freire, DC resistivity near a nematic quantum critical point: Effects of weak disorder and acoustic phonons, *Ann. Phys. (NY)* **419**, 168230 (2020).
- [44] C. A. Marques, L. C. Rhodes, R. Fittipaldi, V. Granata, C. M. Yim, R. Buzio, A. Gerbi, A. Vecchione, A. W. Rost, and P. Wahl, Magnetic-field tunable intertwined checkerboard charge order and nematicity in the surface layer of  $\text{Sr}_2\text{RuO}_4$ , *Adv. Mater.* **33**, 2100593 (2021).

**Supplemental Materials:**  
**Electronic nematic order in the normal state of strontium  
ruthenate**

Ryan Russell,<sup>1</sup> Hari P. Nair,<sup>2</sup> Kyle M. Shen,<sup>3,4</sup> Darrell G. Schlom,<sup>2,4,5</sup> and John W. Harter<sup>1</sup>

<sup>1</sup>*Materials Department, University of California,  
Santa Barbara, California 93106, USA*

<sup>2</sup>*Department of Materials Science and Engineering,  
Cornell University, Ithaca, New York 14853, USA*

<sup>3</sup>*Physics Department, Cornell University, Ithaca, New York 14853, USA*

<sup>4</sup>*Kavli Institute at Cornell for Nanoscale Science, Ithaca, New York 14853, USA*

<sup>5</sup>*Leibniz-Institut für Kristallzüchtung, 12489 Berlin, Germany*



## CONTENTS

I. Experimental methods	2
A. Film growth and characterization	2
B. Static dichroism measurements	3
C. Transient reflectivity measurements	4
D. Dichroism from structural orthorhombicity	4
II. Nematicity across several relaxation timescales	5
A. Orientation dependence	5
B. Pump fluence dependence	6
III. Measurements of film on an LSAT substrate	6
IV. Calculation of pump-induced temperature change	8
V. Derivation of the heat equation	10
VI. Microscopic model of nematic charge order	11
References	12

## I. EXPERIMENTAL METHODS

### A. Film growth and characterization

High-quality superconducting  $\text{Sr}_2\text{RuO}_4$  films were grown on (110)-oriented  $\text{NdGaO}_3$  and (001)-oriented LSAT substrates by molecular-beam epitaxy. The thickness of the films was less than the critical thickness for relaxation, ensuring that they are coherently strained to the substrate. Electrical transport measurements confirm the films are superconducting with a critical temperature of  $T_c \approx 1.4$  K, as shown in Fig. 1. Details of film growth and characterization are provided in Ref. 1.

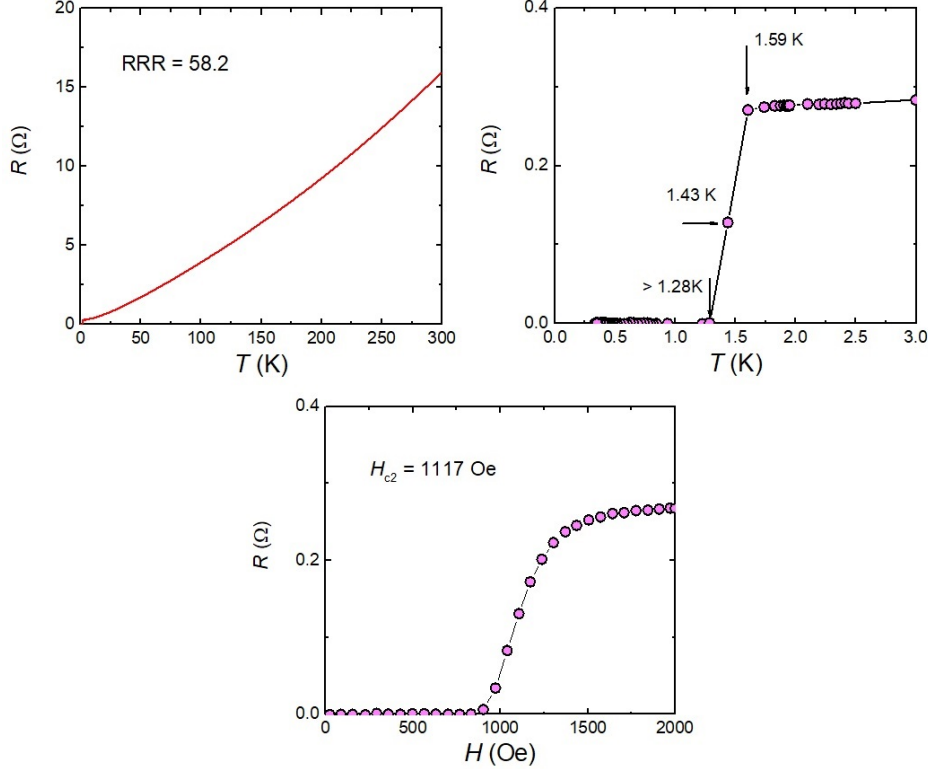


FIG. 1. Superconducting properties of  $\text{Sr}_2\text{RuO}_4$  thin films. Electrical resistance versus temperature of a film grown on (110)  $\text{NdGaO}_3$  shows a residual resistivity ratio (RRR) of 58.2. The superconducting transition at  $T_c \approx 1.4$  K is accompanied by a sharp drop in resistance to zero.  $T_c$  is observed to decrease with applied magnetic field, until superconductivity is completely suppressed above a critical field of  $H_{c2} \approx 1117$  Oe.

## B. Static dichroism measurements

The static optical reflectivity at 800 nm was measured at normal incidence using a linearly polarized probe beam focused to a spot size of  $\sim 30 \mu\text{m}$  at the surface of the sample, with negligible fluence. The same probe beam was later used for time-resolved measurements, but for those measurements a larger probe fluence and oblique incidence were employed. A CMOS camera detector continuously measured the reflected intensity as the sample was steadily warmed from  $\sim 12$  K to  $\sim 300$  K over the course of several hours. Throughout the temperature ramp, the polarization was rapidly switched ( $\sim 1$  Hz) between orientations parallel to the  $a$ -axis and the  $b$ -axis of the sample by mechanically rotating a polarizer. Taking the ratio of these two signals enabled a measurement robust to low-frequency noise

(e.g., laser power fluctuations). Four measurements were collected and averaged for the SRO/NGO sample, and two measurements were averaged for the SRO/LSAT sample.

### C. Transient reflectivity measurements

To probe the low-temperature orientation dependence of the transient reflectivity, samples were cooled using a tabletop optical cryostat to a base temperature of 12 K. An ultrafast laser supplied pump pulses at 500 kHz with a center wavelength of 758 nm, providing a fluence of  $\sim 25 \mu\text{J}/\text{cm}^2$ . Probe pulses with a center wavelength of 800 nm were used to measure the change in reflectivity after a time delay  $t$  controlled by an optical delay stage. Pump pulses were chopped at 500 Hz with a chopper wheel, and the probe signal was measured with a photodiode using a lock-in amplifier. As the sample rotates, so too does the orientation  $\theta$  of the probe polarization with respect to the crystal axes. We emphasize that the pump polarization is always fixed to be orthogonal to the probe, and does not affect the observed nematicity (i.e., the pump polarization does not fix the nematic direction).

### D. Dichroism from structural orthorhombicity

Under the hypothesis that the static dichroism is entirely due to simple  $a \neq b$  structural effects, we would expect a linear proportionality with the substrate orthorhombicity as it changes with temperature. To show this, we expand the reflectivity as a power series in the lattice constants:  $R_a = R_0 + \alpha\delta a + \dots$  and  $R_b = R_0 + \alpha\delta b + \dots$ , where  $\delta a$  and  $\delta b$  are the small deviations of the  $a$  and  $b$  lattice constants from perfect tetragonality. The optical reflectivity anisotropy is then given by

$$\frac{R_a}{R_b} - 1 = \frac{R_0 + \alpha\delta a + \dots}{R_0 + \alpha\delta b + \dots} - 1 = \frac{\alpha}{R_0}(\delta a - \delta b) + \dots$$

We see that the optical reflectivity anisotropy is linearly proportional to the lattice orthorhombicity  $\delta a - \delta b$ . The data, however, show a much larger change in the dichroism than the orthorhombicity as temperature is lowered, as shown in Fig. 1(b) of the main text.

## II. NEMATICITY ACROSS SEVERAL RELAXATION TIMESCALES

To probe the low-temperature orientation dependence of the transient reflectivity, samples were cooled using a tabletop optical cryostat to a base temperature of 12 K. An ultrafast laser supplied pump pulses at 500 kHz with a center wavelength of 758 nm, providing a fluence of  $\sim 25 \mu\text{J}/\text{cm}^2$ . Probe pulses with a center wavelength of 800 nm were used to measure the change in reflectivity after a time delay  $t$  controlled by an optical delay stage. Pump pulses were chopped at 500 Hz with a chopper wheel, and the probe signal was measured with a photodiode using a lock-in amplifier. For long timescales, the transient reflectivity can be fit to

$$\frac{\Delta R(t)}{R} = \sum_{i=1}^3 A_i e^{-t/\tau_i},$$

where the exponential decay terms describe three relaxation processes, each with an amplitude  $A_i$  and a characteristic lifetime  $\tau_i$ . To reveal the nematic symmetry of these relaxation processes, we measured the rotational dependence of the transient reflectivity. As the sample rotates, so too does the orientation  $\theta$  of the probe polarization with respect to the crystal axes. We emphasize that the pump polarization is always fixed to be orthogonal to the probe, and does not affect the observed nematicity (i.e., the pump polarization does not fix the nematic direction).

### A. Orientation dependence

Transient reflectivity curves were measured at 12 K and the characteristic amplitudes  $A_i$  and lifetimes  $\tau_i$  were extracted for the three relaxation processes, each of which showed a marked in-plane anisotropy with nematic two-fold rotational symmetry.  $\tau_1$  (ranging from 0.4 to 6.5 ps) changes most dramatically with  $\theta$ , traversing over an order of magnitude. This shortest timescale is associated with thermalization of hot electrons, as well as electron-phonon interactions as the electrons begin to transfer energy to the lattice. The longer-lifetime relaxation processes,  $\tau_2$  (ranging from 6.4 to 61 ps) and  $\tau_3$  (ranging from 184 to 265 ps), also exhibit nematicity. Figure 2 is a polar plot of the nematicity observed across all timescales. Figure 3(b,d,f) show the same lifetimes  $\tau_i$ , and Fig. 3(a,c,e) show that the two-fold rotational symmetry is also present in the  $A_i$  amplitudes, each having a minimum near  $\theta = 90^\circ$  (polarization along the  $b$ -axis).



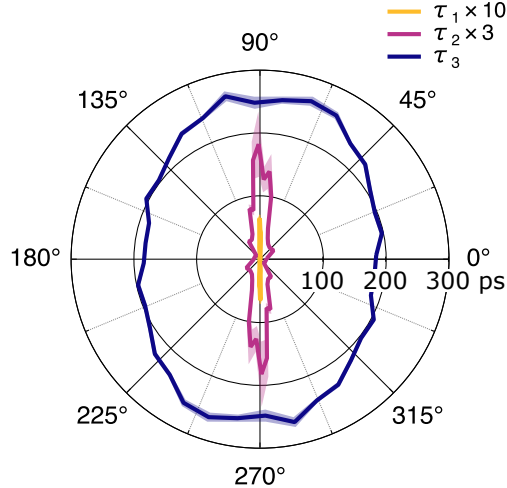


FIG. 2. Two-fold symmetry with respect to angle  $\theta$  is observed across all three relaxation lifetimes.  $\theta = 0^\circ$  corresponds to a probe polarization oriented along the  $a$ -axis.  $\tau_1$  exhibits a particularly strong anisotropy, spanning an order of magnitude. Note that  $\tau_1$  and  $\tau_2$  are scaled by a factor of 10 and 3, respectively. Shaded regions indicate one standard deviation in the extracted lifetime parameters from least-squares fits of the data.

### B. Pump fluence dependence

We also studied the effects of pump fluence on our measurements. The pump fluence was adjusted via the average pump power (with a fixed laser pulse repetition rate and spot size). We used pump powers ranging from 0.5 to 6 mW, spanning over an order of magnitude (Fig. 4). We find that  $\Delta R/R$  increases approximately linearly with increasing pump fluence up to 6 mW, with slight evidence of saturation at the highest fluence. Two-fold symmetry is retained across the entire time-delay range studied, from 0 to 500 ps. Strikingly, we observe the pump fluence to significantly affect the magnitude of the observed nematicity at short (sub-picosecond) time delays. Figure 5 illustrates this difference.

### III. MEASUREMENTS OF FILM ON AN LSAT SUBSTRATE

Transient reflectivity measurements were performed on a  $\text{Sr}_2\text{RuO}_4$  thin film grown on an LSAT substrate, which is tetragonal and induces no uniaxial strain. Figure 6(a) shows that in the absence of uniaxial strain, the in-plane anisotropy of the transient reflectivity vanishes. Figure 6(b) compares the transient reflectivity of SRO/LSAT to a particular

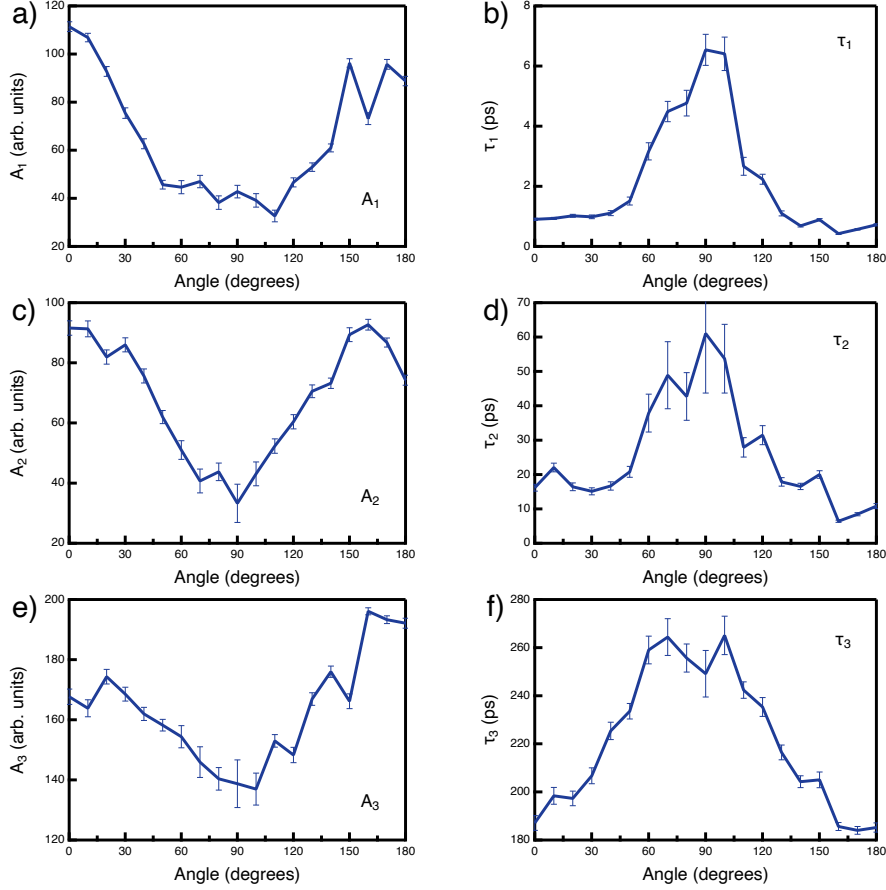


FIG. 3. Fit parameters as a function of sample orientation angle  $\theta$ . (a), (c), and (e) show the amplitudes  $A_i$  of the equilibration processes, each with a minimum at  $90^\circ$  (along the  $b$ -axis). (b), (d), and (e) show the relaxation lifetimes  $\tau_i$ , each peaked at  $90^\circ$ . Two-fold nematic rotational symmetry is seen in both  $A_i$  and  $\tau_i$  for all three relaxation processes.

weighted average of the transient reflectivity of SRO/NGO at the  $0^\circ$  (maximum) and  $90^\circ$  (minimum) orientations. The similarity of the two responses using an approximate 3:1 ratio is curious, suggesting a nontrivial averaging of nematic domains within the SRO/LSAT sample. Without an epitaxial strain field setting a preferred global alignment direction for the domains, it is possible that the polarization direction of the pump and/or probe is preferentially aligning them. Under this scenario, we would not observe rotational anisotropy (because the pump and probe polarization rotate with  $\theta$ ), but we would observe a domain imbalance.

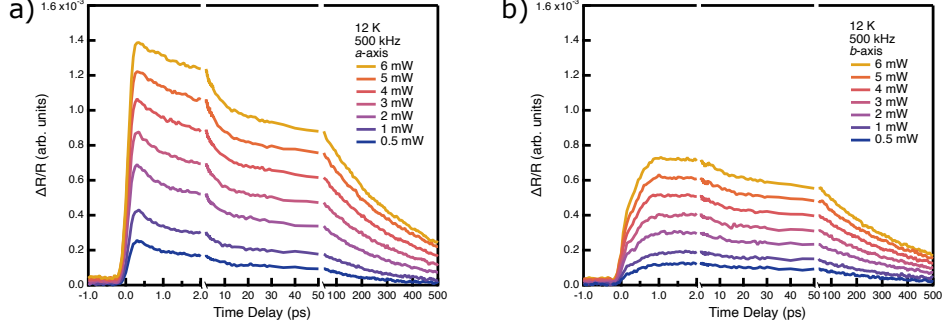


FIG. 4. Transient reflectivity traces acquired using several selected average pump powers. The magnitude of the transient reflectivity is observed to grow approximately linearly with increasing pump power. (a) Transient reflectivity for  $\theta = 0^\circ$  (along the  $a$ -axis). (b) Transient reflectivity for  $\theta = 90^\circ$  (along the  $b$ -axis). Nematicity is observed at all pump powers measured.

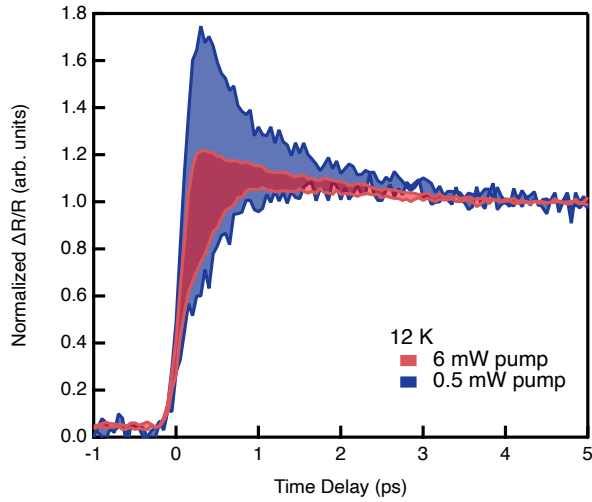


FIG. 5. Pump power dependence of nematicity at 12 K. Traces are normalized such that  $\Delta R/R = 1$  at 5 ps. A larger pump power is seen to suppress nematicity. The shaded area represents the difference in the transient response between  $\theta = 0^\circ$  and  $90^\circ$  for the lowest pump fluence (blue) and highest pump fluence (red).

#### IV. CALCULATION OF PUMP-INDUCED TEMPERATURE CHANGE

The transient reflectivity data were obtained using a pump fluence of  $\sim 25 \mu\text{J}/\text{cm}^2$  (0.5 mW average chopped power at a repetition rate of 500 kHz over a spot size of diameter  $\sim 100 \mu\text{m}$ ). We seek to calculate the energy deposited per formula unit under such a fluence. We assume the pump is absorbed following Beer's law,  $I(z) = I_0 e^{-\alpha z}$ , with an

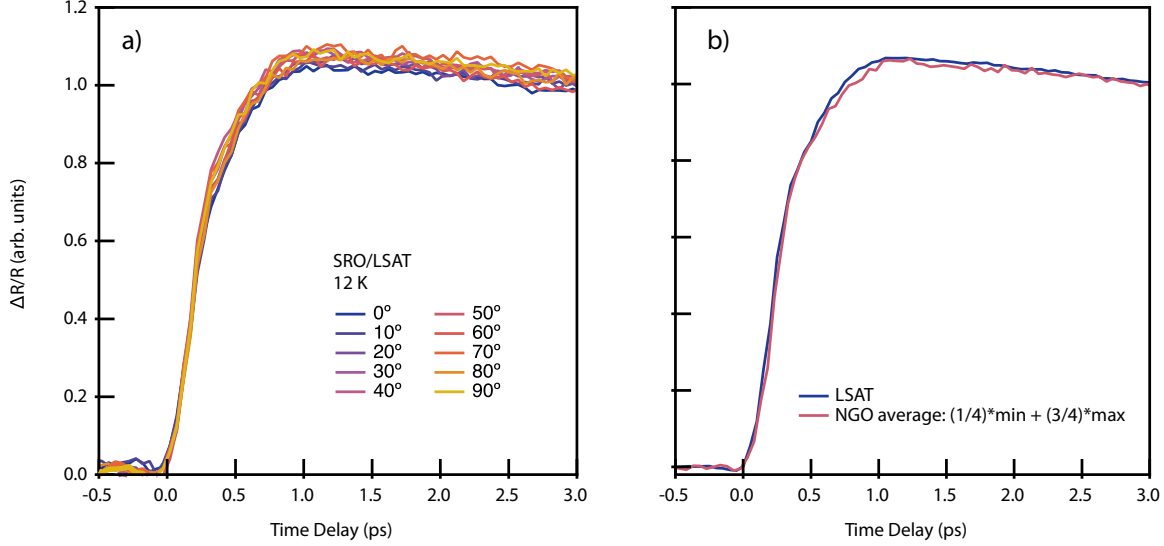


FIG. 6. Transient reflectivity measurements of  $\text{Sr}_2\text{RuO}_4$  grown on a tetragonal LSAT substrate. (a) Absence of nematic anisotropy in the transient optical response. (b) Comparison of SRO/LSAT data with a weighted average of SRO/NGO data.

absorption coefficient given by  $\alpha = 4\pi\kappa/\lambda$ . From Ref. 2, we determine the index of refraction of  $\text{Sr}_2\text{RuO}_4$  at 800 nm to be  $n + i\kappa = 1.2 + 0.98i$ , from which we calculate an absorption length  $\alpha^{-1} = 65$  nm. Using the Fresnel equations, we also calculate the surface reflection loss for  $S$ -polarized light with angle of incidence  $12^\circ$  to be  $R = 0.18$ . The in-plane area of one unit cell of  $\text{Sr}_2\text{RuO}_4$  is  $a^2 = (3.86 \text{ \AA})^2$  and the  $\text{RuO}_2$  planes are separated by a distance  $c/2 = 6.36 \text{ \AA}$ . A naïve calculation of the energy deposited per formula unit yields

$$\Delta E_0 = 25 \mu\text{J}/\text{cm}^2 \times (3.86 \text{ \AA})^2 \times \frac{6.36 \text{ \AA}}{65 \text{ nm}} \times (1 - 0.18) = 1.87 \text{ meV}.$$

A more careful analysis, however, shows that a factor of  $2/3$  is needed to correct this value. This arises from the fact that the intensity of the pump decays exponentially with depth below the surface of the sample. We are measuring a property, the pump-induced change in reflectivity  $\Delta R$ , that depends functionally on the deposited energy at different depths:  $\Delta R(\Delta E_0 e^{-\alpha z})$ . The probe beam, measuring this property at a specific depth  $z$ , must travel a total distance  $2z$  within the material, through which its intensity also decays. Integrating over all depths, the average signal that is measured in the experiment is

$$\Delta R_{\text{avg}} = \frac{\int_0^\infty \Delta R(\Delta E_0 e^{-\alpha z}) e^{-2\alpha z} dz}{\int_0^\infty e^{-2\alpha z} dz} = 2 \int_0^1 \Delta R(\Delta E_0 x) x dx.$$



We make the additional assumption, verified experimentally, that  $\Delta R$  is linearly proportional to pump intensity. Thus,  $\Delta R(\Delta E_0 x) = \Delta R(\Delta E_0)x$ , from which we find

$$\Delta R_{\text{avg}} = 2\Delta R(\Delta E_0) \int_0^1 x^2 dx = \frac{2}{3}\Delta R(\Delta E_0) = \Delta R(2/3 \times \Delta E_0).$$

The net result is that the *measured* change in reflectivity  $\Delta R_{\text{avg}}$  corresponds to the change in reflectivity calculated for a pump with 2/3 the incident intensity. Thus, we use  $\Delta E = 2/3 \times \Delta E_0 = 1.25$  meV. An electronic heat capacity  $C(T) = \gamma T$  corresponds to an internal energy  $U(T) = \gamma T^2/2$ . Applying conservation of energy, we find  $U(T_{\text{initial}}) + \Delta E = U(T_{\text{final}})$ , whose solution is  $T_{\text{final}} = \sqrt{T_{\text{initial}}^2 + (2\Delta E/\gamma)}$ . Finally, we set  $\Delta T_{\text{max}} = T_{\text{final}} - T_{\text{initial}}$ . Using the electronic heat capacity coefficient  $\gamma = 3.88 \times 10^{-4}$  meV/K<sup>2</sup> reported in Ref. 3, we find  $(2\Delta E/\gamma) \approx (80 \text{ K})^2$ .

## V. DERIVATION OF THE HEAT EQUATION

The assumption of a universal temporal evolution of the nematic temperature is derived from the fundamental heat equation  $dQ/dt = g(T_0 - T)$ , where  $dQ/dt$  is the amount of heat flowing into a subsystem at instantaneous temperature  $T(t)$  that is connected to a thermal bath at temperature  $T_0(t)$  through a “weak link” with coupling constant  $g$ . Here, this coupling is due to the electron interactions that drive equilibration of the hot electron thermal bath with the nematic degrees of freedom. Treating the collective excitations of the nematic order (e.g. amplitude fluctuations) as simple bosonic Einstein oscillators, we have a nematic heat capacity  $C = dQ/dT \approx \text{constant}$  (valid in the semi-classical limit), and so we may write  $dT/dt = k(T_0 - T)$  with temperature-independent coefficient  $k = g/C$ . Finally, to normalize different temperature scales, we divide both sides of this equation by a constant (namely  $\Delta T_{\text{max}}$ , determined for each starting temperature) to give  $df/dt = k(f_0 - f)$ , which is the universal temporal evolution to which we fit the data. The semi-classical high temperature limit with constant nematic heat capacity is justified because the frequency  $\omega_0$  of the nematic amplitude mode is measured in our work to be  $\hbar\omega_0/k_B \approx 40$  K, which is much smaller than the minimum electronic temperature after pump absorption ( $> 80$  K). This means that during and after equilibration,  $k_B T \gg \hbar\omega_0$  and the nematic order is in the Einstein heat capacity high-temperature limit, making our analysis self-consistent.

## VI. MICROSCOPIC MODEL OF NEMATIC CHARGE ORDER

To develop a microscopic model of intra-unit-cell electronic nematic order in  $\text{Sr}_2\text{RuO}_4$ , we perform a mean-field analysis of the Emery model of the  $\text{RuO}_2$  plane, closely following Ref. 4. Instead of duplicating their detailed analysis, however, here we simply identify the principal differences. First, because we are interested in Ru  $d_{xy}$  orbitals (instead of Cu  $d_{x^2-y^2}$  orbitals relevant to  $\text{CuO}_2$  planes), the kinetic energy part of the Hamiltonian (associated with hopping between the transition metal  $d$ -orbital and oxygen  $p$ -orbitals) is different. Second, because we are only interested in phase boundaries, we ignore other interaction parameters (namely,  $U_d$  and  $V_{pd}$ ) that do not change the boundary locations. We define a  $1000 \times 1000$  square grid of  $k$ -points, and at each point numerically diagonalize the Hamiltonian matrix

$$\mathcal{H}_{\mathbf{k}} = \begin{pmatrix} \xi_x & \gamma_2(\mathbf{k}) & \gamma_1(k_x) \\ \gamma_2(\mathbf{k}) & \xi_y & \gamma_1(k_y) \\ \gamma_1(k_x) & \gamma_1(k_y) & \xi_d \end{pmatrix},$$

where

$$\begin{aligned} \gamma_1(k_i) &= -2t_{pd} \sin(k_i/2), \\ \gamma_2(\mathbf{k}) &= -4t_{pp} \sin(k_x/2) \sin(k_y/2), \\ \xi_x &= -(2V_{pp} - U_p/4)\eta - \mu, \\ \xi_y &= +(2V_{pp} - U_p/4)\eta - \mu, \\ \xi_d &= \Delta - \mu, \end{aligned}$$

with all hopping and interaction parameters defined as in Fig. 4(a) of the main text. Band filling (relative to the van Hove singularity) is implicitly controlled through the chemical potential  $\mu$ . Following Ref. 5, we take  $t_{pd} = 1.5$  eV,  $t_{pp} = 0.4$  eV, and  $U_p = 4.4$  eV.  $\Delta$  is the charge-transfer energy, which we take to be 0.5 eV to best match the density-functional theory calculated band structure of  $\text{Sr}_2\text{RuO}_4$  (e.g., Fig. 1 of Ref. 6). Our results, however, are insensitive to the exact values of these parameters.  $\eta = (n_{x\uparrow}^p + n_{x\downarrow}^p) - (n_{y\uparrow}^p + n_{y\downarrow}^p)$  is the nematic charge order parameter, which is finite when there is unequal occupation of the  $p_x$  and  $p_y$  orbitals. We define the grand potential per unit cell

$$\omega = -2k_B T \sum_{\alpha, \mathbf{k}} \ln [1 + \exp(-\xi_{\alpha, \mathbf{k}}/k_B T)] + (V_{pp} - U_p/8)\eta^2,$$

where  $\xi_{\alpha,\mathbf{k}}$  are the eigenvalues of the matrix  $\mathcal{H}_{\mathbf{k}}$ . To find the phase boundaries, we set

$$\left. \frac{\partial^2 \omega}{\partial \eta^2} \right|_{\eta=0} = 0$$

and solve this equation for  $V_{pp}$  at each temperature and band filling. These phase boundaries are shown in Fig. 4(c) and (d) of the main text. Our results are very similar to those of Ref. 4, with the major difference being a shift and reversal of direction of the filling axis.

- 
- [1] H. P. Nair, J. P. Ruf, N. J. Schreiber, L. Miao, M. L. Grandon, D. J. Baek, B. H. Goodge, J. P. C. Ruff, L. F. Kourkoutis, K. M. Shen, D. G. Schlom. Demystifying the growth of superconducting  $\text{Sr}_2\text{RuO}_4$  thin films. *APL Mater.* **6**, 101108 (2018).
  - [2] D. Stricker, J. Mravlje, C. Berthod, R. Fittipaldi, A. Vecchione, A. Georges, D. van der Marel. Optical Response of  $\text{Sr}_2\text{RuO}_4$  Reveals Universal Fermi-Liquid Scaling and Quasiparticles Beyond Landau Theory. *Phys. Rev. Lett.* **113**, 087404 (2014).
  - [3] A. P. Mackenzie, S.-I. Ikeda, Y. Maeno, T. Fujita, S. R. Julian, G. G. Lonzarich. The Fermi Surface Topography of  $\text{Sr}_2\text{RuO}_4$ . *J. Phys. Soc. Jpn.* **67**, 385 (1998).
  - [4] M. H. Fischer, E.-A. Kim. Mean-field analysis of intra-unit-cell order in the Emery model of the  $\text{CuO}_2$  plane. *Phys. Rev. B* **84**, 144502 (2011).
  - [5] K. Rościszewski, A. M. Oleś. Charge-transfer model for the electronic structure of layered ruthenates. *Phys. Rev. B* **91**, 155137 (2015).
  - [6] D. Singh. Relationship of  $\text{Sr}_2\text{RuO}_4$  to the superconducting layered cuprates. *Phys. Rev. B* **52**, 1358 (1995).